High-resolution surface wave tomography of the European crust and uppermost mantle from ambient seismic noise — Source link

Yang Lu, Laurent Stehly, Anne Paul

Related papers:

- High-resolution surface-wave tomography from ambient seismic noise.

- Surface Wave Tomography of the Alps Using Ambient-Noise and Earthquake Phase Velocity Measurements

- Processing seismic ambient noise data to obtain reliable broad-band surface wave dispersion measurements

- The AlpArray Seismic Network: A Large-Scale European Experiment to Image the Alpine Orogen

- Emergence of broadband Rayleigh waves from correlations of the ambient seismic noise.

High-resolution surface wave tomography of the European crust and uppermost mantle from ambient seismic noise

Yang Lu, Laurent Stehly, Anne Paul, Alparray Working Group

HAL Id: hal-02156637
https://hal.archives-ouvertes.fr/hal-02156637v2

Submitted on 23 Nov 2020

High-resolution surface wave tomography of the European crust and uppermost mantle from ambient seismic noise

Yang Lu, Laurent Stehly, Anne Paul and AlpArray Working Group*

Université Grenoble Alpes, CNRS, IRD, IFSTTAR, ISTerre, Grenoble 38041, France. E-mail: yang.lu@univ-grenoble-alpes.fr

SUMMARY

Taking advantage of the large number of seismic stations installed in Europe, in particular in the greater Alpine region with the AlpArray experiment, we derive a new high-resolution 3-D shear wave velocity model of the European crust and uppermost mantle from ambient-noise tomography. The correlation of up to 4 yr of continuous vertical-component seismic recordings from 1293 broad-band stations (10°W–35°E, 30°N–75°N) provides Rayleigh wave group velocity dispersion data in the period band 5–150 s at more than 0.8 million virtual source–receiver pairs. 2-D Rayleigh wave group velocity maps are estimated using adaptive parametrization to accommodate the strong heterogeneity of path coverage. A probabilistic 3-D shear wave velocity model, including probability densities for the depth of layer boundaries and S-wave velocity values, is obtained by nonlinear Bayesian inversion. A weighted average of the probabilistic model is then used as starting model for the linear inversion step, providing the final V_s model. The resulting S-wave velocity model and Moho depth are validated by comparison with previous geophysical studies. Although surface wave tomography is weakly sensitive to layer boundaries, vertical cross-sections through our V_s model and the associated probability of the presence of interfaces display striking similarities with reference controlled-source seismology (CSS) and receiver function sections across the Alpine belt. Our model even provides new structural information such as an ∼8 km Moho jump along the CSS ECORS-CROP profile that was not imaged by the reflection data due to poor penetration across a heterogeneous upper crust. Our probabilistic and final shear wave velocity models have the potential to become new reference models of the European crust, both for crustal structure probing and geophysical studies including waveform modelling or full-waveform inversion.

Key words: Europe; Tomography; Seismic noise.

1 INTRODUCTION

The European lithosphere is characterized by strong heterogeneity at a scale of a few tens to a few hundreds of kilometres, in particular along its southern margin due to the long history of Tethyan subductions and collisions with Africa and the Mediterranean microplates. Until recently, reference seismic models of the European crust have been built by combining results of active and passive seismic experiments carried out at regional scale [EuCRUST-07 (Tesauro *et al.* 2008), Crust1.0 (Laske *et al.* 2013) and EPcrust Molinari & (Morelli 2011)]. Seismic models of the European mantle are derived separately using these crustal velocity models as *a priori* information (Boschi *et al.* 2009; Schivardi & Morelli 2011; Legendre *et al.* 2012; Zhu *et al.* 2015). Probing the entirety of such

a heterogeneous lithosphere at a suitable resolution, for instance of a few tens of kilometres in the upper crust and with a single method, remains a challenge.

In the heart of Europe, the Alps have been intensely studied by geologists for more than a century, and they provide a unique natural laboratory to advance our understanding of orogenesis and its relationship to present and past mantle dynamics. While many concepts that underlie current studies of mountain belts and convergence dynamics were born in the Alps, the dynamics of this complex belt is not yet understood due to a lack of high-quality geophysical data. A first step in the re-evaluation of deep structures and processes that occur beneath the Alps is high-resolution imaging of the crust and uppermost mantle.

In the last decades, the structure of the Alpine crust has been probed at regional scale by controlled-source seismic profiles (from west to east: ECORS-CROP, Nicolas *et al.* 1990; NFP-20, Pfiffner *et al.* 1997; TRANSALP, Lüschen *et al.* 2004), local earthquake tomography (LET) studies (e.g. Paul *et al.* 2001; Diehl *et al.* 2009)

and receiver function studies (e.g. Kummerow *et al.* 2004; Spada *et al.* 2013; Zhao *et al.* 2015).

Since the pioneering work by Shapiro *et al.* (2005), ambient-noise tomography (ANT) has proven to be particularly efficient to image the crust and uppermost mantle at the scale of continents provided that continuous noise records are available at dense arrays of seismic stations. Indeed, experimental, theoretical and laboratory studies have shown that the Rayleigh wave between two seismic stations can be reconstructed from the cross-correlation of seismic noise records at the stations, basically turning each station to a source of seismic waves (Weaver & Lobkis 2001, 2002; Campillo & Paul 2003; Wapenaar 2004; Roux *et al.* 2005; Larose *et al.* 2006; Sánchez-Sesma *et al.* 2006). In the Alpine region, Stehly *et al.* (2009), Li *et al.* (2010), Verbeke *et al.* (2012) and Molinari *et al.* (2015) used noise correlations to compute Rayleigh wave phase and group velocity, and to derive isotropic shear wave velocity models. Fry *et al.* (2010) studied the azimuthal anisotropy of Rayleigh wave phase velocities in the crust of the western Alps.

Since the first ANT at the European scale conducted by Yang *et al.* (2007), numerous new permanent broad-band seismic stations have been installed in Europe and their data are being distributed by the European Integrated Data Archive (EIDA) facility (https://www.orfeus-eu.org/data/eida/). Moreover, seismologists from 10 European countries have joined their effort in the AlpArray seismic network that covers the broader Alpine region with a dense (average spacing 50 km) and homogeneous array of more than 600 seismic stations, filling the gaps between permanent stations with temporary stations (http://www.alparray.ethz.ch/en/home/, Hetényi *et al.* 2018). These data provide a unique opportunity to image the crust and uppermost mantle beneath the greater Alps at an unprecedented resolution. In addition, the use of records from permanent stations surrounding the broader Alpine region together with stations in the Alps not only allows probing the Alpine mantle to larger depth but also provides the opportunity to compute a velocity model of the crust and uppermost mantle beneath most of Europe. This is the main goal of the present work, which uses up to 4 yr of data from the 1293 stations shown in Fig. 1.

Through the processing of noise records at these stations, we measured Rayleigh wave velocities at several hundreds of thousands of station pairs (depending on the considered frequency), from which we derived 2-D group velocity maps in the 5–150 s period band. We finally obtained a 3-D V_s model of the crust and uppermost mantle beneath Europe by inverting for a local 1-D V_s profile in each cell.

Since the solution of this inverse problem is non-unique, we further developed the grid search approach by Stehly *et al.* (2009) and Macquet *et al.* (2014) to obtain a probabilistic 3-D V_s model. The probabilistic model gives at each location (longitude, latitude and depth) a probabilistic distribution of V_s, and the probability to have a layer boundary. This is done using a Bayesian approach that consists in exploring the whole model space assuming a three-layer crust above a mantle half-space. Starting from this probabilistic 3-D V_s model, we then derived a final 3-D V_s model by linear inversion.

Imaging sharp discontinuities with surface waves such as the Rayleigh waves reconstructed from ambient-noise correlations is an issue because their velocities are not strongly sensitive to the depth of layer boundaries. We show that our model, which includes probabilistic information on the depth estimates of layer boundaries, provides reliable information on Moho depth or thickness of sedimentary basins.

In summary, the originality of our work compared to previous ANT studies of the Alpine region (Stehly *et al.* 2009; Li *et al.* 2010; Verbeke *et al.* 2012; Molinari *et al.* 2015) is threefolds: (1) We performed ANT at a broader scale covering a large part of Europe with a particular emphasis on the Alpine region using unprecedented density of data; (2) ANT is usually restricted to the 5–50 s period band that is suitable for probing the crust. Here, we were able to measure Rayleigh wave velocity to 50 s, making it possible to get a reliable V_s model for both the crust and the uppermost mantle; (3) we derived a 3-D V_s probabilistic model of the Alps, including the depth to layer boundaries.

This paper is organized as follows: we first present how data have been processed and the correlations computed. We then present group velocity maps obtained across Europe in the 5–150 s period band. In Section 4, we present the 3-D shear wave velocity model obtained from the inversion of group velocity maps using a two-step data-driven inversion algorithm. Finally, we discuss some geological implications of our model for the Alpine region.

2 DATA PROCESSING

We used up to 4 yr (July 2012–June 2016) of continuous seismic noise recorded by 1293 broad-band stations (Fig. 1), located in the area (10°W–35°E, 30°N–70°N; see Section 7 for the origin of data). The data were obtained through the EIDA. As shown by Fig. 1, the best station coverage is achieved in the Alpine and Apennine regions, where the average interstation distance is ∼50 km.

Before computing the correlations for each receiver pair, we pre-processed the noise recorded by each station in two main steps. First, each daily record was detrended, band-pass filtered (0.005–2 Hz), corrected from the instrument response and decimated to 5 Hz. Second, we followed the processing scheme proposed by Boué *et al.* (2014) to remove earthquakes and other transient events, and to decrease the contribution of dominant noise sources. Each daily record was split into 4-hr segments. Within each 4-hr segment, we iteratively removed energetic signals with amplitude four times greater than the standard deviation. Within each day, we removed 4-hr segment when its energy distribution is uneven and its energy is 1.5 times greater than the daily average. The remaining segments were whitened in the frequency domain.

For each of the 0.8 million station pairs, we computed the cross-correlation of up to 4 yr of continuous noise records by segment of 4 hr. The resulting cross-correlations were then stacked. Supporting Information Fig. S1 shows the histogram of the number of months used to compute the stacked correlations. Fig. 2 shows the cross-correlations computed between station DAVOX in Switzerland and the other 1292 stations, sorted by interstation distance in the 10–20 s and 40–80 s period bands. The cross-correlations are plotted in such a way that the causal (positive time) and acausal parts (negative time) correspond to seismic waves propagating eastwards and westwards, respectively. In the 10–20 s period band, the Rayleigh wave emerges clearly with an average velocity ∼2.9 km s^{-1} in both the causal and acausal parts. We note that the amplitude of the Rayleigh wave is larger in the causal than in the acausal part. This is consistent with a dominant noise source located in the northern Atlantic Ocean (Stehly *et al.* 2006; Pedersen & Krüger 2007; Yang & Ritzwoller 2008). In the period band 40–80 s, Rayleigh wave has a velocity ∼3.9 km s^{-1}. The correlations are more symmetric in this period band, because the propagation of surface waves is global, and the same noise source contributes simultaneously to both sides of the correlations.
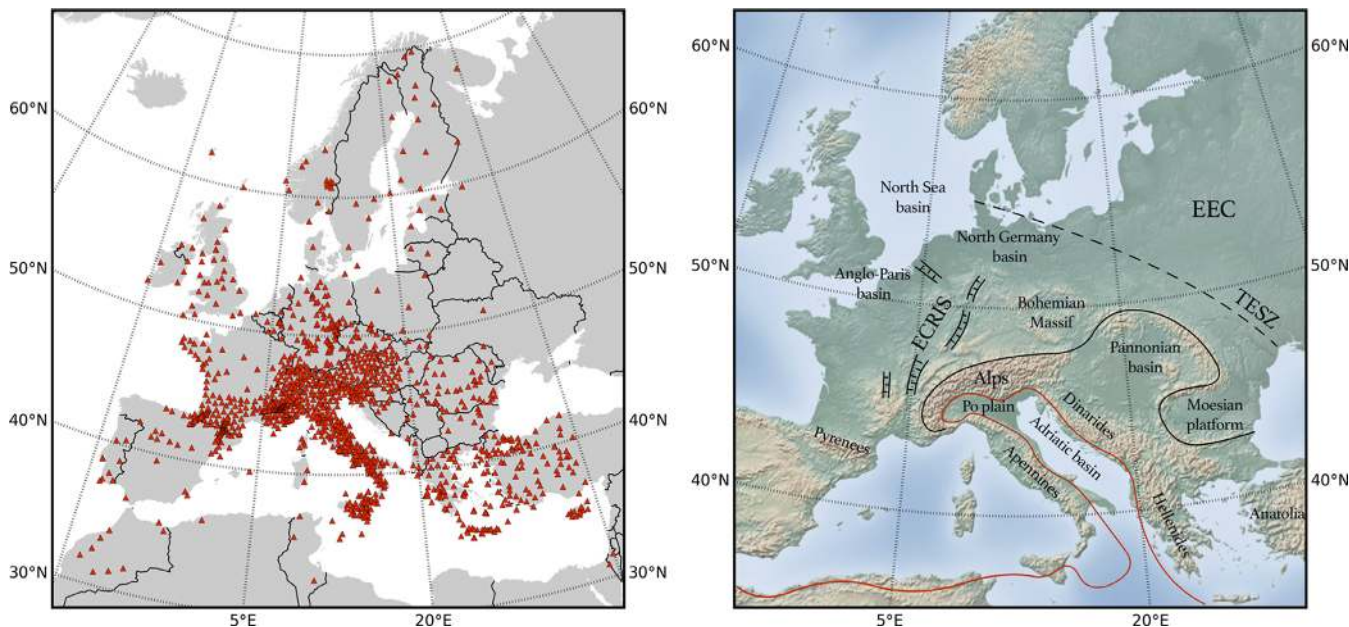
Figure 1. Left: map of the 1293 broad-band seismic stations (the red triangles) used in this study. Right: main geological units discussed in the paper. ECRIS, European Cenozoic Rift System (modified from Dèzes *et al.* 2004); EEC, Eastern European Craton; TESZ, Trans-European Suture Zone (modified from Pharaoh 1999). The black line outlines the Alpine Front, and the red line the boundary between the Eurasian and African plates (modified from Platt 2007).

3 GROUP VELOCITY TOMOGRAPHY

3.1 Group velocity measurement and selection

We used multiple-filter analysis (Dziewonski *et al.* 1969; Herrmann 1973) to compute the Rayleigh wave group velocity dispersion curves in the 5–150 s period band. We adapted the filter width to the interstation distance to accommodate the trade-off between time and frequency domain resolution (Levshin *et al.* 1989). Group velocity measurements were performed separately on the causal and acausal parts for each station pair. We selected the most reliable group velocity measurements for each period by applying three criteria: (1) We considered only station pairs separated by 3–50 wavelengths. The lower limit aims at avoiding interference of Rayleigh waves between the causal and acausal parts, while the higher limit eliminates long paths that bring less information on the medium. (2) We evaluated the signal-to-noise ratio (SNR) of the causal and acausal Rayleigh waves in the period band of interest. The SNR is defined as the ratio of the peak amplitude of the Rayleigh waves to the standard deviation of the coda waves (Stehly *et al.* 2009). We kept only station pairs with SNR greater than 5 for both the causal and acausal parts. (3) We discarded all station pairs with group velocities measured on the causal and acausal parts of the correlations differing by more than 0.2 km s^{-1}. This criterion rejects measurements strongly biased by a heterogeneous distribution of noise sources.

Table 1 presents the statistics of the selection procedure at representative periods. After selection, we kept 2 per cent to 30 per cent of the station pairs depending on the period. The uncertainty on the group velocity is defined as the difference between the causal and acausal measurements. This uncertainty mainly arises from: (1) the non-homogeneous noise source distribution that results in asymmetric cross-correlations; (2) the compromise between resolution in the time domain and resolution in the frequency domain in the time–frequency analysis. As a whole, group velocity measurements have an average uncertainty in the range 0.05–0.09 km s^{-1}.

Finally, we averaged the causal and acausal Rayleigh wave group velocities of the selected station pairs to obtain the final measurements. As an example, Fig. 3 shows the dispersion curve measured between DAVOX and SLIT.

3.2 Inversion for 2-D group velocity maps: method

At target periods, selected Rayleigh wave group velocities were inverted to 2-D tomographic maps using a linearized inversion algorithm based on the ray theory. Following Boschi & Dziewonski (1999), the inverse problem is defined as

$$
\begin{bmatrix} A \\ \mu G \end{bmatrix} * x = \begin{bmatrix} d \\ 0 \end{bmatrix}, \tag{1}
$$

where $A*x = d$ is the 'standard' ill-conditioned forward problem and $\mu G*x = 0$ is the regularization term.

In the first relation, the matrix A contains for each path the path length of Rayleigh waves within each cell. Vector d contains the difference between the observed traveltime and the computed traveltime derived from a homogenous initial velocity model. We chose the mean of all measurements as the initial velocity at a given period. Vector x contains the desired slowness perturbations.

The second relation defines the roughness regularization, which stabilizes the system by minimizing a first-order solution roughness for neighbouring cells. The construction of the damping operator G is discussed into detail by Schaefer *et al.* (2011). The roughness regularization coefficient μ was determined near the maximum curvature of the 'L-curve' to compromise the trade-off between data fitting and regularization (Hansen 2001). The linear problem was solved in a least-squares sense. Its solution was approximated via an iterative LSQR algorithm (Paige & Saunders 1982).

In view of the strong heterogeneity of the data coverage, we implemented an adaptive parametrization using cell sizes of 0.6°, 0.3° and 0.15° depending on the path density. To that end, we first meshed our region of interest with 0.6° cells. Areas with more than 100 paths per cell were then discretized using 0.3° cells. We further
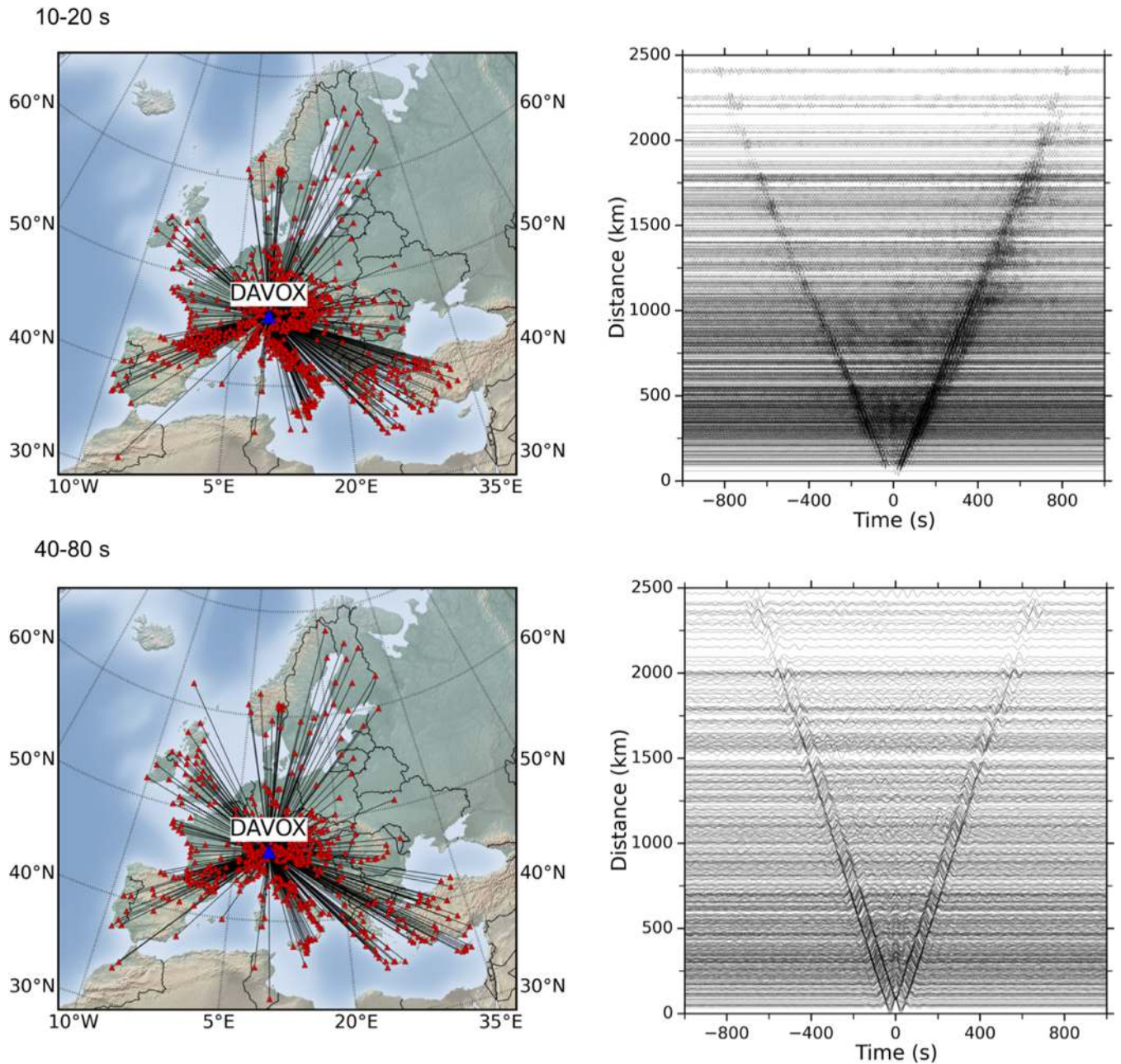
Figure 2. Selected cross-correlations computed between DAVOX and the other stations as a function of the interstation distance, filtered in the period bands 10–20 s (top panels) and 40–80 s (bottom panels). Supporting Information Fig. S2 shows cross-correlations in period bands 20–40 s and 80–150 s.

Table 1. Number of group velocity measurements kept after each step of the selection procedure. Error refers to the average uncertainty at that period.

Period (s)	8	15	25	40	125
Distance	395 206	593 555	654 319	628 433	330 814
SNR	222 071	366 315	370 312	175 846	22 483
Symmetry	100 852	232 314	189 369	118 548	15 294
Error (km s^{-1})	0.066	0.057	0.083	0.080	0.083

refined the mesh to 0.15° in areas with more than 100 paths per 0.3° cell. Fig. 4 shows the parametrization used to compute the 8 s group velocity map. Using this adaptive parametrization, we optimized local resolution while reducing the complexity of the problem and the computational cost (Spakman & Bijwaard 2001; Schaefer *et al.* 2011).

The resolution of 2-D tomographic result is evaluated by multi-scale checkerboard tests (see Supporting Information Fig. S3). For the upper crust, the resolution reaches 0.3° in the Alpine region. At Moho depth, the resolution reaches 0.9° in the Alpine region and it is better than 1.8° in most of the area.
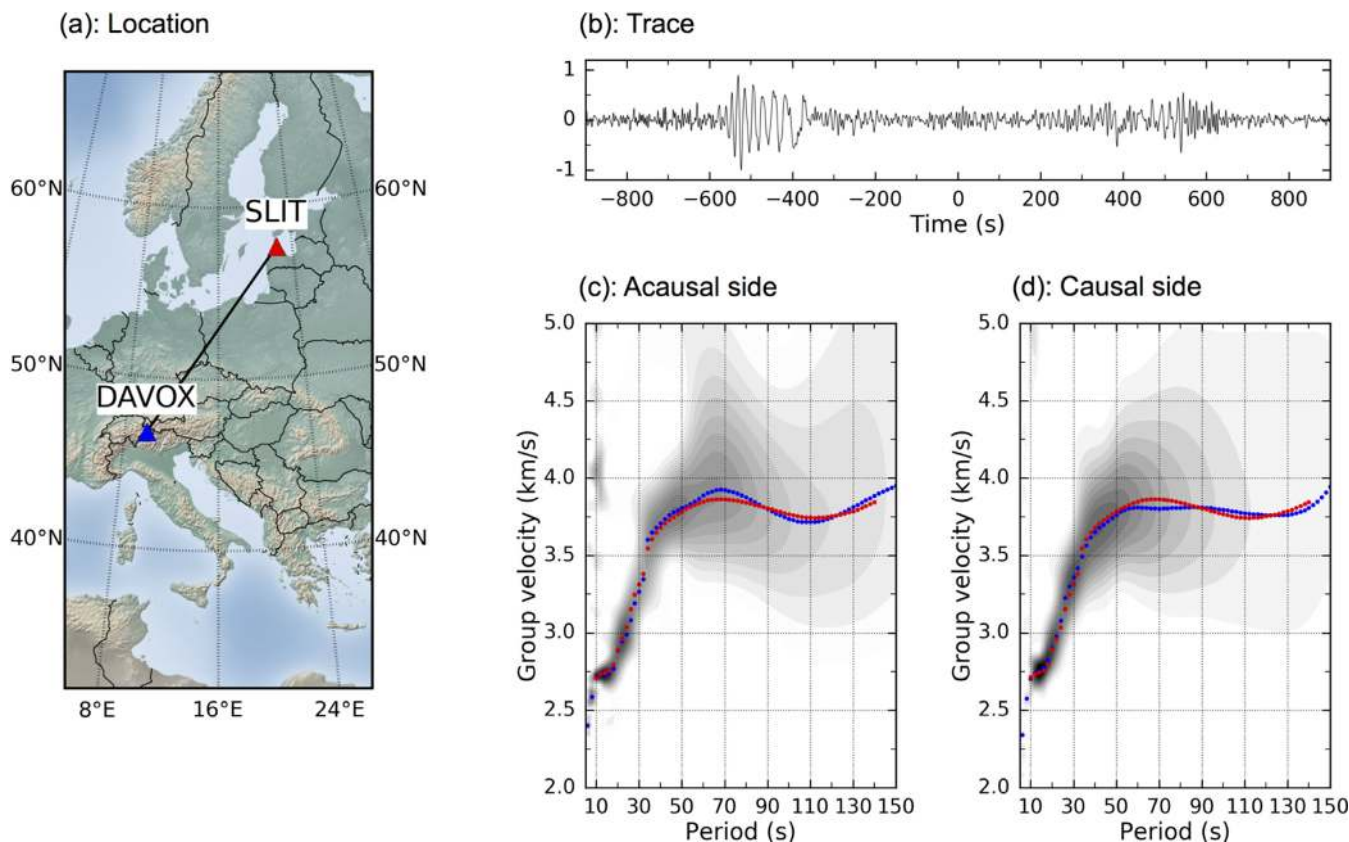
(a): Location

(b): Trace

(c): Acausal side

(d): Causal side

Figure 3. Group velocity dispersion curves measured for station pair DAVOX–SLIT. (a) Location map. (b) Noise correlation waveform. (c–d) Results of multiple-filter analysis for the causal and acausal parts. The shaded background displays energy in the time–frequency domain. The group velocity curve is plotted as blue dots, and the final dispersion curve (average of the causal and acausal parts) is shown as a red dotted line.

The uncertainty of the inversion is evaluated using Jackknifing tests (see Supporting Information Fig. S4).

3.3 Group velocity maps

The depth sensitivity of Rayleigh waves depends on their dominant period. Between 5 and 150 s, Rayleigh waves are mostly sensitive to depths ranging from 4 to 200 km, which almost correspond to the whole lithosphere.

At 8 s (Fig. 5a), Rayleigh waves are mostly sensitive to the upper crust (5–8 km). Thus, we observe low velocity anomalies associated with sedimentary basins such as the North Sea basin, the northwest Mediterranean Sea, the Po plain, the Pannonian basin and the Moesian platform. The northwest Mediterranean Sea and the Po plain exhibit velocities as low as $1.5 \, \mathrm{km \, s^{-1}}$. On the other hand, high velocity anomalies are mainly related to orogenic belts including the Alps as well as Variscan massifs such as the Bohemian Massif. A strong high velocity anomaly characterizes the Eastern European Craton (EEC; including the Baltic shield, the Russian platform and the Ukrainian platform). At 40 s (Fig. 5b), we image low velocity anomalies along the Alps, the Apennines, the Dinarides and the Hellenides, which are due to the deep crustal roots of these mountain ranges. At 125 s period (Fig. 5c), Rayleigh waves probe upper-mantle structures, in particular the Trans-European Suture Zone (TESZ), which is the boundary between the high-velocity lithosphere of the EEC and the low-velocity lithosphere of the West European platform.

4 3-D SHEAR WAVE VELOCITY MODEL

4.1 Inversion for shear wave velocity

Our aim is to derive two 3-D V_s models of Europe: (1) A probabilistic model resulting from an exhaustive grid search which gives at each location the probability distribution of V_s and the probability of the presence of a layer boundary. We shall show that this model is suitable for structural interpretation. (2) A final model computed from the probabilistic model that provides at each location and depth a unique value of V_s. This model may be used as a starting point of further geophysical studies such as full-waveform tomography.

To that end, we extract the local Rayleigh wave group velocity dispersion curve at each cell of our model from the group velocity maps presented in the previous section. Each dispersion curve is inverted to get a local 1-D V_s model. All 1-D V_s models are finally assembled in a quasi-3-D final V_s model. However, the 1-D inversion is still challenging since the solution of the inverse problem is non-unique. We choose to use a two-step data-driven inversion algorithm.

First, we build a probabilistic model using a Bayesian approach: at each cell of the model, assuming a four-layer structure, we search the whole model space by comparing the local Rayleigh wave dispersion curve with the dispersion curves associated with a library of 8 million of 1-D V_s models. This comparison is done in the 5–70 s period band. It provides a probabilistic model that includes at each cell/depth the probability distribution of the S-wave velocity and the probability of the presence of a layer boundary.

Second, we further derive a unique V_s model at each cell by performing an additional linear inversion that uses the whole Rayleigh
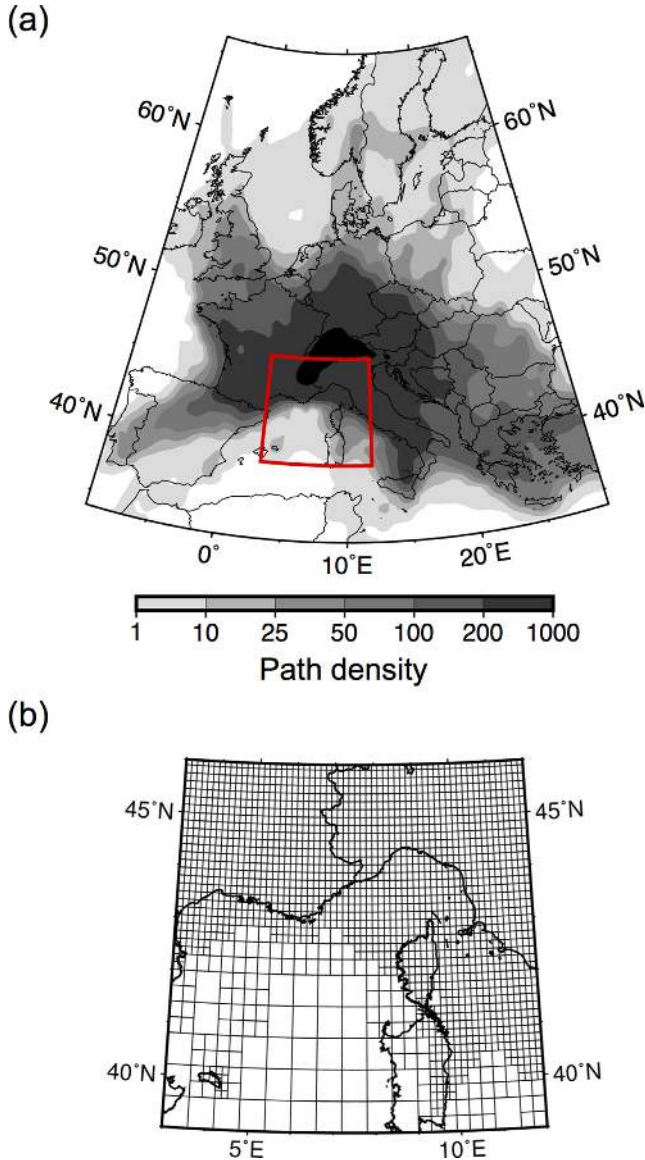
Figure 4. Example of adaptive parametrization at period of 8 s. (a) Number of paths crossing each $0.15° \times 0.15°$ cell. (b) Meshing resulting from the three-level adaptive parametrization in a selected region (the red frame in a).

wave dispersion curve (5–150 s). This second step is mainly used to constrain the velocity in the uppermost mantle. The inversion method is presented in details in the following sections.

4.1.1 Computation of a probabilistic V_s crustal model using a Bayesian algorithm

Our Bayesian algorithm is derived from the approach used by Bodin *et al.* (2012) and Shen *et al.* (2013) for joint inversion of surface wave dispersion and receiver functions (RFs). Since our observations only contain local Rayleigh wave group velocity dispersion, we simplify the original approach in two main aspects. First, we simplify the inversion parametrization assuming that at each cell the model can be described by a four-layer model (see Table 2). Second, we simplify the likelihood function assuming that the local Rayleigh wave velocities at different periods are independent from

each other and have equal uncertainties. In view of the relative simple parametrization, we can directly search over the full model space without using sophisticated optimization techniques. To that end, we compute a library of 8×10^6 synthetic four-layer 1-D V_s models and their corresponding Rayleigh wave group velocity dispersion curves. Each model includes a sedimentary layer, an upper crust, a lower crust and a half-space representing the uppermost mantle. Each layer is parametrized by its thickness and S-wave velocity. We restrict the range of thicknesses and velocities to plausible values following the reference models Crust1.0 (Laske *et al.* 2013) and EPcrust (Molinari & Morelli 2011). Table 2 presents the ranges of explored parameters. *P*-wave velocities and densities are converted from V_s using empirical formulae (Ludwig *et al.* 1970; Brocher 2005).

At each cell, we evaluate the misfit between the local dispersion curve d_{obs} and each of the synthetic dispersion curve $g(m)$ of our library using the following misfit function:

$$\Phi(m) = (g(m) - d_{obs})^T C_e^{-1} (g(m) - d_{obs}), \tag{2}$$

where C_e is the covariance matrix. Similar to Shen *et al.* (2013), we ignore off-diagonal elements of the covariance matrix by assuming local Rayleigh wave velocities at different periods are independent. Hence, C_e is only defined by diagonal elements, which are the square of uncertainties of the observational dispersion curve at the corresponding period. This is further simplified by using a unique uncertainty σ for all periods,

$$C_e = \begin{bmatrix} \sigma^2 & 0 & 0 \\ 0 & ... & 0 \\ 0 & 0 & \sigma^2 \end{bmatrix}. \tag{3}$$

Following Bodin *et al.* (2012), we compute the probability that each synthetic model explains the observed dispersion curve by assuming a Gaussian-type likelihood function:

$$p(d_{obs}|m) = \frac{1}{\sqrt{|C_e|}} \exp(-\frac{\Phi(m)}{2}). \tag{4}$$

By substituting eqs (2) and (3) into eq. (4), we obtain

$$p(d_{obs}|m) = \frac{1}{\sigma^N} \exp\left(-\frac{(g(m) - d_{obs})^2}{2\sigma^2}\right), \tag{5}$$

where N is the number of measured periods. The difficulty lies in the quantitative estimate of uncertainty σ. To address this question, we use a 'hierarchical approach' and treat σ as an additional parameter (Bodin *et al.* 2012). In this way, the inversion procedure performs a grid search for σ and gives a probability value for each possible σ. This self-determined uncertainty not only represents the observational error but also takes into account the misfit of the synthetic model.

This procedure gives us the probability that each of the synthetic models explains the local dispersion curve for each cell of the model. By analysing this information, we can derive the probability to have an interface and a given S-wave velocity at each location/depth as documented by Fig. 6.

4.1.2 Linear inversion for the final V_s model

From the probabilistic model, we build an initial V_s model by averaging at each cell the 8×10^6 synthetic models weighted by their probability of occurrence. As a consequence, the obtained initial V_s model exhibits velocity gradients instead of sharp discontinuities. Due to our four-layer model initial assumption, the initial V_s models have a constant velocity in the mantle, which may lead to
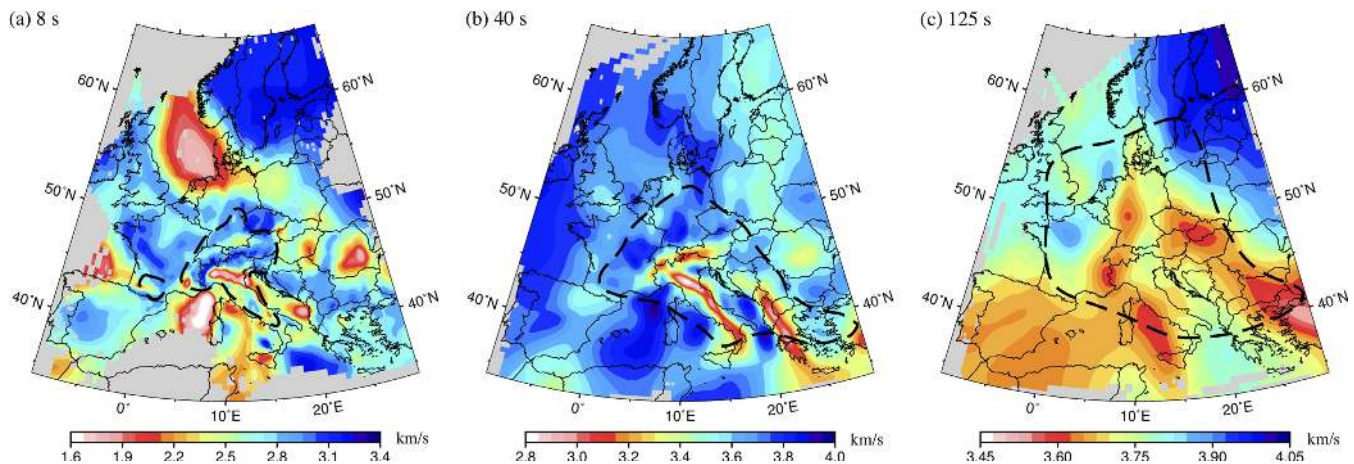
Figure 5. Group velocity maps at representative periods 8, 40 and 125 s. We plot only cells crossed by more than 10 paths. The black dashed lines enclose the well-resolved area as defined in Supporting Information Fig. S3 from the checkerboard tests. Supporting Information Fig. S5 shows group velocity maps at periods 5, 15, 25 and 75 s.

Table 2. Priori parameter settings of the Bayesian inversion.

	Thickness (km)	V_s (km s^{-1})
First layer (sediment)	0–16	1.7–2.7
Second layer (upper crust)	0–24	2.7–3.5
Third layer (lower crust)	2–42	3.5–4.1
Fourth layer (mantle)	inf	4.1–4.7
Increment	1.0	0.2
Uncertainty (σ)	0.01–0.20 km s^{-1}	

unrealistic results after linear inversion. Thus, we assume that V_s gradually increases in the mantle from the obtained value below Moho to 4.77 km s^{-1} at 400 km in agreement with the global model PREM (Dziewonski & Anderson 1981). The crustal and mantle parts of the initial model are discretized with intervals of 1 and 10 km, respectively. At each cell, we then perform a linear inversion of the observed local Rayleigh wave dispersion curve in the 5–150 s period band (Herrmann 2013). The linear inversion mainly updates the upper-mantle velocities.

The robustness of the final V_s model is assessed quantitatively by calculating at each cell the misfit between the observed dispersion curve and the one associated with the V_s model in different period bands (see Supporting Information Fig. S6). In most of the studied region, the rms error is less than 0.04 km s^{-1}.

4.1.3 Example of V_s models obtained in the Molasse basin

Fig. 6 shows an example of 1-D shear velocity inversion in the Molasse basin (8.5°E, 47.5°N) to illustrate our inversion procedure. Fig. 6(b) presents the probabilistic crustal model at this location. The probability distribution of V_s (shaded grey area) illustrates the non-uniqueness of the inversion of Rayleigh wave dispersion data. However, we note that at each depth, the range of plausible V_s extends over less than 0.2 km s^{-1}. Fig. 6(c) presents the probability for a layer boundary to exist at the given depth. The probability function has two local maxima at ∼32.5 and ∼37.5 km that might be interpreted as Moho depth. This ambiguity illustrates the difficulty of mapping interfaces using ANT due to: (1) the stronger sensitivity of Rayleigh waves to layer velocities than to velocity contrasts across interfaces, (2) our assumption that structure can be described locally by a four-layer model while the medium has a complex structure and (3) the intrinsic non-uniqueness of the solution of the inverse

problem. In the example of Fig. 6, we define the Moho depth from the probabilistic V_s model as the weighted mean position rather than that of maximum probability. The resulting Moho depth is 36.5 ± 3.5 km while the uncertainty is defined by the standard deviation.

Fig. 6(e) shows the final V_s model obtained from the probabilistic model after the linear inversion. As outlined in the previous section, the final V_s model (the blue line) and the weighted average of the probabilistic V_s models (the red line) are similar in the crust and quite different at mantle depth. Fig. 6(f) displays the gradient of the final shear velocity profile as a function of depth. A strong gradient is indicative of a sharp transition zone at a layer boundary. We approximate the boundary depth as the central position of the transition zone, and its thickness gives the uncertainty on the depth estimate. The obtained Moho depth is 35 ± 5 km.

4.2 Results: 3-D shear wave velocity model

Fig. 7 presents three depth slices at 10, 30 and 150 km in the final 3-D V_s model. The thick-black dashed lines outline the well-resolved area at each depth according to the criteria discussed in Section 3.3.

In the upper crust (10 km), the areas of lowest velocities (2.5–2.9 km s^{-1}) correspond to thick sedimentary basins such as the North Sea basin, the North German basin, the Po plain, the Adriatic basin and the Moesian platform (Fig. 7a).

The 30-km depth slice (Fig. 7b) underlines variations in crustal thickness, with low velocities (3.5 km s^{-1}) in the mountain belts (Pyrenees, Alps, Apennines, Dinarides and Hellenides) and high velocities (>4.1 km s^{-1}) in the areas of stretched continental crust that crosses Western Europe from the northwesternmost Mediterranean Sea to the western Baltic Sea and North Sea Rift System including the European Cenozoic Rift System.

The 150-km depth slice (Fig. 7c) displays striking similarities with published mantle velocity models obtained from earthquake records (Boschi *et al.* 2009; Schivardi & Morelli 2011; Legendre *et al.* 2012; Zhu *et al.* 2015). The high velocities (>4.4 km s^{-1}) of the EEC strongly contrast with the lower velocities (<4.3 km s^{-1}) of Western Europe across the TESZ. Low *S*-wave velocities (∼4.2 km s^{-1}) characterize the upper mantle of the western Mediterranean Sea, a roughly south–north stripe beneath the European Cenozoic Rift System and another stripe from the
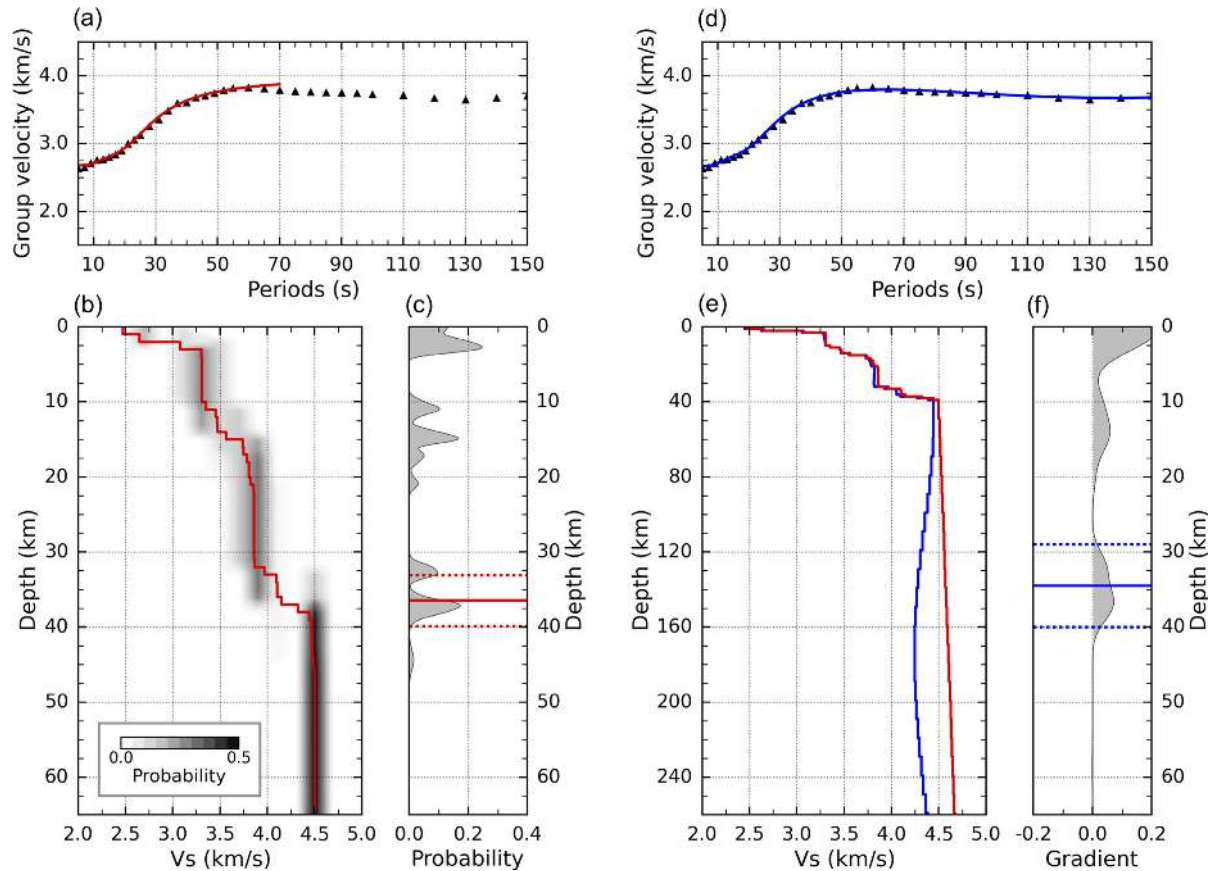
Figure 6. Computation scheme and results of the two-step inversion of dispersion data for shear wave velocity at a cell located in the Molasse basin (8.5°E, 47.5°N). Left: nonlinear Bayesian inversion step (to 70 s maximum period). Right: linear inversion step (to 150 s period). (a) Observed (the black triangles) and predicted (the red curve) Rayleigh wave dispersion curves using the Bayesian inversion. (b) Resulting V_s model displayed as *a posteriori* probability distribution of the *S*-wave velocity at each depth (grey background) obtained from the Bayesian inversion. The weighted average of the V_s models is shown as the red curve. (c) Probability for a layer boundary to be located at a given depth (the grey shaded curve) and estimate of Moho depth with uncertainty (the continuous and dotted red lines). (d) Observed and predicted dispersion curves after the linear inversion (the black triangles and blue solid line, respectively). (e) V_s model predicted by the weighted average of the probabilistic model (the red solid line) and final result of the linear inversion (the blue solid line). The two models are similar in the crust and differ in the mantle. (f) Depth gradient of the final V_s model (the shaded curve) and estimated Moho depth (the blue solid line) defined as the central position of the transition zone from crustal velocity to mantle velocity.
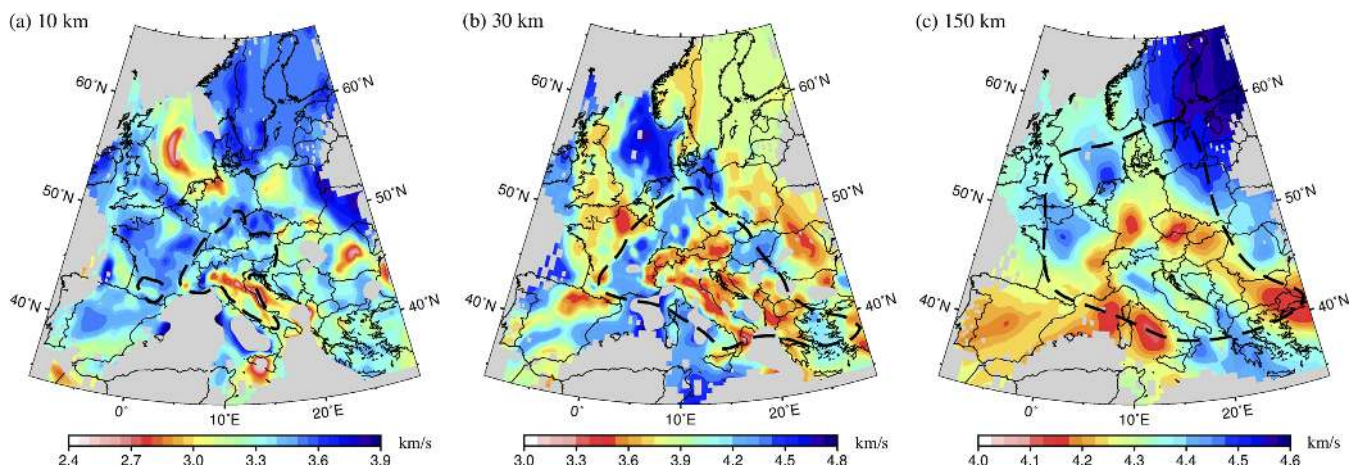

Figure 7. Depth slices in the final V_s model at 10 km (a), 30 km (b) and 150 km (c). We only display cells with more than 10 crossing ray paths at 8 s period. Moreover, we discard cells with rms error greater than $0.06 \, \mathrm{km \, s^{-1}}$ in the short-, intermediate- and long-period ranges, respectively, for depth slices at 10, 30 and 150 km (Supporting Information Fig. S6). As in Fig. 5, the black dashed lines enclose the well-resolved area as defined from the checkerboard tests (Supporting Information Fig. S3). Supporting Information Fig. S7 displays depth slices at 5, 20, 40 and 75 km.

Pannonian basin to northwestern Anatolia. Conversely, the upper mantle of the Anglo–Paris basin and the North Sea grabens have high V_s (4.4–4.5 km s^{-1}) as well as the deep roots of orogens such as the Apennines, the central–eastern Alps and the Dinaric–Hellenic system. Our V_s model is well-resolved to such unusual depths for ANT, thanks to a good coverage by long ray paths and long duration of observation to enhance the SNR at long periods. The vertical resolution is however, poorer than in the crust because long-period Rayleigh waves are sensitive to a broader range of depth than short-period waves used to probe the crust.

5 DISCUSSION: A FOCUS ON THE ALPINE REGION

The result of this work is a new, high-resolution V_s model of the crust and uppermost mantle for most of the European region. It is however, out of the scope of this paper to discuss its results at such a large scale. Therefore, we focus the discussion on the Alpine region which, thanks to the dense station coverage by permanent seismic networks and temporary arrays such as the AlpArray seismic network, is the best-resolved area of our study region. The resolution of the area is 0.3° at 8 s (most sensitive to upper crust) and 0.9° at 40 s (most sensitive to structure at Moho depth).

5.1 Moho depth map

The Moho discontinuity is a first-order parameter in geophysical and geodynamic models of mountain belts, which draws attention in seismic tomography studies of the lithosphere. Moreover, the depth to the crust–mantle boundary in the Alpine region has been measured by numerous seismic methods including controlled-source seismology (CSS), RF analyses and ANTs that lead to a large set of published Moho map models at the European scale (Grad & Tiira 2009; Molinari & Morelli 2011) or in the Alpine region (Waldhauser *et al.* 1998; Stehly *et al.* 2009; Spada *et al.* 2013; Molinari *et al.* 2015). In Fig. 8, we compare our Moho depth maps (Figs 8d–f) with two reference models for the European plate (Fig. 8a: Grad & Tiira 2009; Fig. 8b: Molinari *et al.* 2015) and the most up-to-date regional Moho depth map derived from CSS and RF data in the greater Alpine region (Fig. 8c: Spada *et al.* 2013). There is no single definition of the seismic crust–mantle boundary. We therefore, show three different maps that consider the Moho as a first-order velocity change in Fig. 8(d; see Section 4.1.1 and Fig. 6c), a transition zone in Fig. 8(e; see Section 4.12 and Fig. 6f) and the top of upper-mantle velocities (isovelocity of 4.2 km s^{-1}) in Fig. 8(f).

The main features of our three Moho maps (Figs 8d–f) are similar, except in the region of the Ivrea body (IB in Fig. 8e) which is a high-density, high-velocity body located at crustal depth and interpreted as a slice of serpentinized Adriatic upper mantle (Closs & Labrouste 1963; Nicolas *et al.* 1990). The shallow Moho on top of the IB shows up well in Fig. 8(e; transitional Moho) because it is characterized by a strong velocity gradient, albeit with anomalously low V_s in the mantle slice due to serpentinization.

The comparison with three reference models shows that our Moho maps include more details, thanks to our much denser data set and hence higher resolution. For example, the narrow and very-shallow Moho of the IB shows up in Fig. 8(e), and to a lesser extent in Fig. 8(d) while it is only visible in Fig. 8(c). Similarly, the model by Spada *et al.* (2013) is the only one that displays the thick crust of the Northern Apennines as well as in our Moho models. As Molinari *et al.* (2015) obtained a similar result with ANT, we confirm again

the large Moho depth values estimated in the northern Apennines by Piana Agostinetti & Amato (2009) from RF data (~52 km maximum crustal thickness). The division of the Alpine arc into two regions of thick crust separated by a narrow zone of thinner crust in the central Alps (namely beneath the Ossola–Tessin region, see Fig. 8e) is more visible in our Moho maps than in any of the three reference models, in particular in fig. 8(c) by Spada *et al.* (2013). To the west and the north of the Alpine arc, the shallow Moho of the European Cenozoic Rift System is also more visible in our model.

5.2 Cross-sections along reference profiles (Cifalps, ECORS-CROP, Transalp)

In this section, we compare our results to CSS and RF results along three reference cross-sections of the southwestern (Cifalps), northwestern (ECORS-CROP) and eastern Alps (Transalp). The locations of the cross-sections are shown in Fig. 9(a).

5.2.1 Cifalps receiver function profile (AA' in Figs 9b-d)

The Cifalps experiment is a roughly linear profile of broad-band seismic stations installed for 14 months from the Rhone valley (southern France) to the Po plain (northern Italy) across the southwestern Alps. Figs 9(b)–(d) compare our results to those of the RF analysis by Zhao *et al.* (2015) and the LET by Solarino *et al.* (2018). They show that the depth to the European Moho estimated from ANT is in good agreement with the Moho depth estimated from RFs (the thick black dotted line) beneath the Frontal Penninic thrust (FPT) and its surroundings (150–210 km). Further to the east, the northeastward-dipping European Moho imaged as a weak P–S converted phase on the RF profile at depths >45 km shows up with ANT. At the western end of the profile, the RF Moho is deeper than the ANT Moho by 5–8 km beneath the Southeast Basin. The use of an inappropriate velocity model in the migration of the RF data may explain this difference. The Moho structure estimated from ANT beneath the Po plain and on top of the IB (abscissae > 270 km) correlates well with the RF Moho. The V_s anomaly of the IB in Fig. 8(b) has a similar shape as the high V_p anomaly imaged from LET in Fig. 8(d), with a vertical western boundary.

5.2.2 CSS profile ECORS-CROP (BB' in Figs 9e–f)

Figs 9(e)–(f) display a comparison between our results and the migrated line-drawing of the ECORS-CROP CSS experiments in the northwestern Alps (Thouvenot *et al.* 1990; Sénéchal & Thouvenot 1991). In the European side, west of the FPT, the agreement between the ANT Moho and the ECORS-CROP Moho imaged as the base of the reflective lower crust is striking. Further east, the ANT also delineates the European Moho at larger depths (45–55 km) beneath the internal zones, in the part of the section where it was detected by wide-angle profiling but not by near-vertical reflection data. The ANT detects a step of 8 km in the European Moho a few kilometres to the west of the FPT. A similar step can be observed between the Moho of the ECORS-CROP near-vertical reflection section beneath the Belledonne Massif at 38 km depth and the wide-angle Moho reflections at 48–50 km, a few kilometres further east (the thick dashed lines in Fig. 9f). A mid-crustal boundary is detected by the ANT at 25 km depth at the same location as the base of the thick band of reflections in the upper crust of the internal zones. Further east, our ANT also detects the top of the IB at ~10 km beneath the westernmost Po plan, and a step-by-step increase of the Adriatic Moho
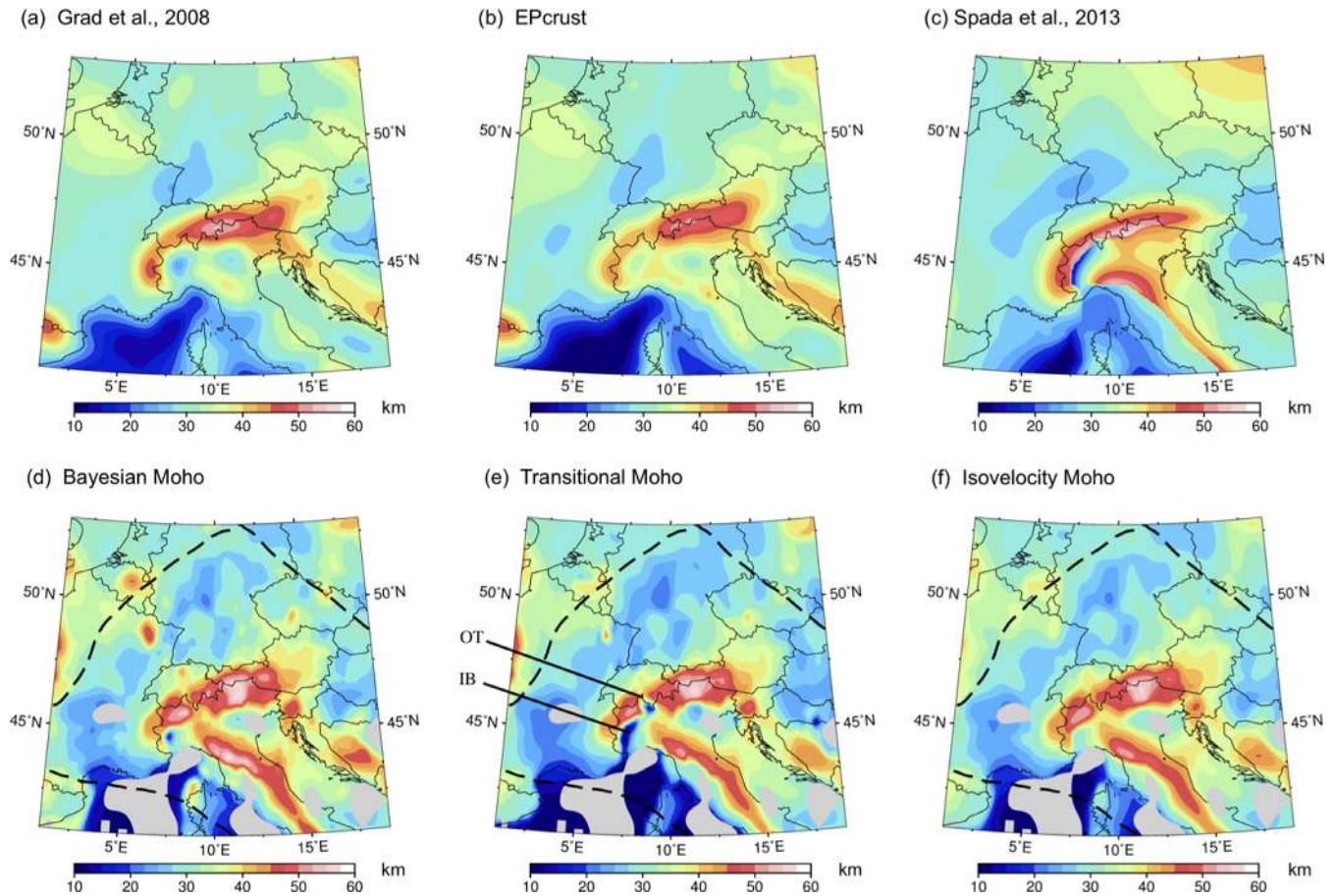
Figure 8. Moho depth maps from previous works (a: Grad & Tiira 2009; b: model EPcrust, Molinari & Morelli 2011; c: Spada *et al.* 2013) and derived from this study (d: using the probability for a boundary to be located at the given depth; e: using the depth gradient of V_s; f: using the isovelocity 4.2 km s^{-1}). In each map (d)–(f), the black dashed line encloses the well-resolved area defined at 40 s period (see Supporting Information Fig. S3). Besides, we also discard areas with rms error greater than 0.06 km s^{-1} in the intermediate-period band (see Supporting Information Fig. S6). IB, Ivrea body; OT, Ossola–Tessin region. Supporting Information Figure S8 shows two 3-D views of the Bayesian Moho depth map that emphasize its strong and rapid lateral changes.

depth that is similar to the results of the ECORS-CROP wide-angle experiment reported by Thouvenot *et al.* (1990). The shape of the IB as depicted by the V_s section in Fig. 9(e) is similar to the Cifalps section (Fig. 9b) with a vertical western boundary.

5.2.3 Receiver function and CSS profile Transalp (CC' in Figs 9g–i)

The third reference cross-section is the Transalp profile in the eastern Alps (Transalp Working Group 2002). The experiment combined active (near-vertical seismic profiling, wide-angle profiles, cross-line refraction profiles; Lüschen *et al.* 2004) and passive (RF analysis; Kummerow *et al.* 2004) seismic imaging. Figs 9(g)–(i) compare our V_s model (Fig. 9g) and probability of occurrence of interfaces (Fig. 9h) with the results of the near-vertical reflection profile (migrated line-drawing) and RF section (Fig. 9i). In the northern half of the profile, our Moho fits very well the European Moho imaged by near-vertical reflection profiling. This is not the case in the Adriatic side of the section, south of the suture (the so-called 'Sub-Tauern ramp' of Lüschen *et al.* 2004). The northernmost Adriatic Moho is well-delineated by ANT, but 10–15 km deeper than the reflection Moho. Further south, the ANT does not give a well-defined Moho because a large set of crustal models with different Moho depths fits equally well the observed Rayleigh

wave dispersion data. Among the three reference cross-sections, the Adriatic side of the Transalp profile is the only example of a clear misfit between our ANT crustal structure and the results of active or passive seismic imaging. Nevertheless, Fig. 9(i) shows that the reflection profile and the RF analysis also disagree on the depth of the Adriatic Moho, in particular close to the suture. Our results may even suggest that the European crust underthrusts the Adriatic crust, if we assume that the clear interface at ∼60 km depth in the Adriatic side is the continuation of the European Moho. This hypothesis was not favoured by the Transalp team in spite of some clues of overlapping Adriatic and European Mohos in the RF sections (fig. 2 in Kummerow *et al.* 2004).

6 CONCLUSION

Taking advantage of the rapidly increasing number of broad-band seismic stations in Europe in the last 10 yr, including the AlpArray temporary seismic network in the greater Alpine region, we compiled a large data set including up to 4 yr of vertical-component continuous seismic records from 1293 stations. Daily records were cross-correlated and stacked for ∼0.8 million station pairs. For each station pair, we measured Rayleigh wave group velocity from the cross-correlation function in the period band 5–150 s and we
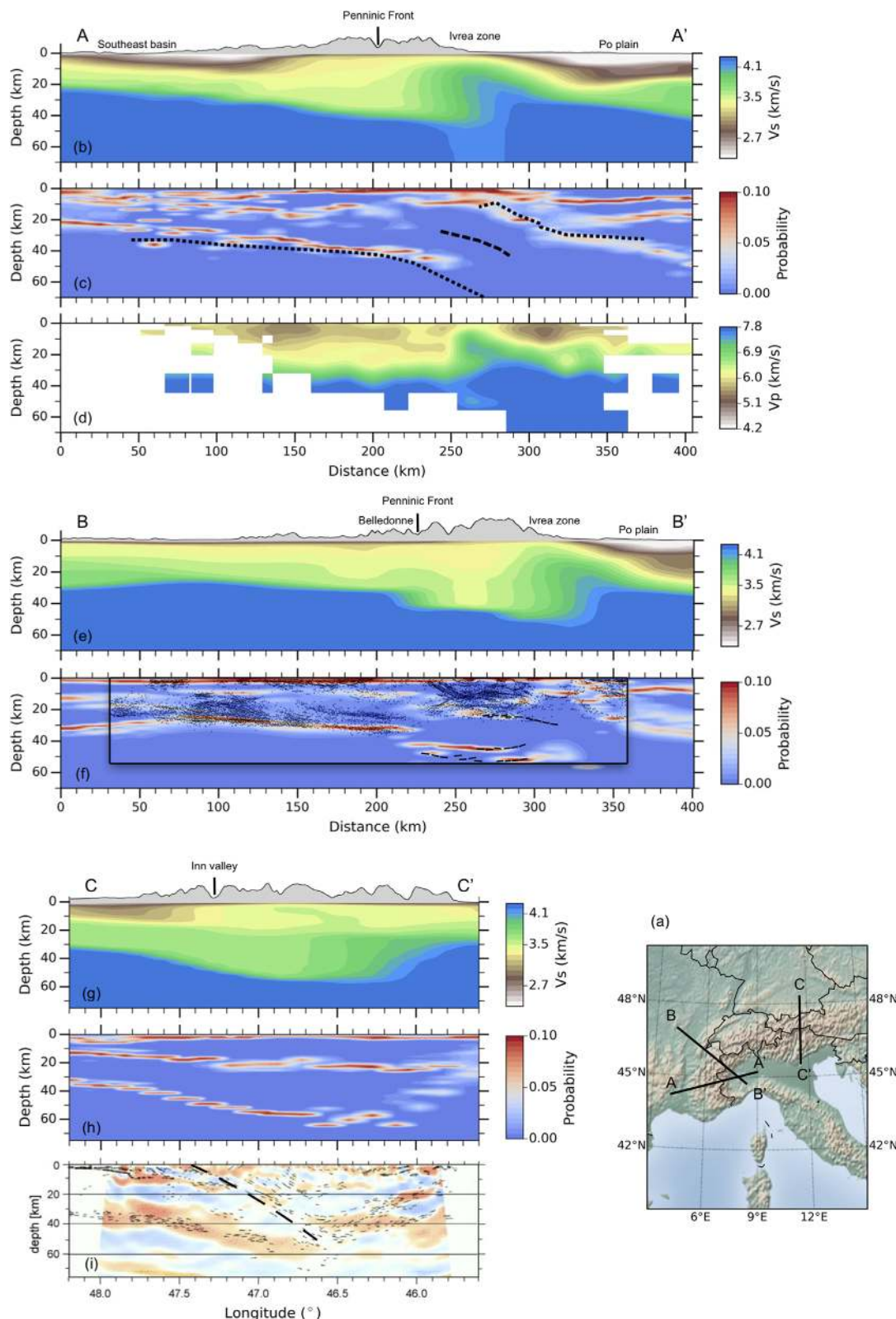
Figure 9. Depth sections along three representative profiles across the Alpine mountain range: Cifalps (AA', b–d), ECORS-CROP (BB', e–f) and Transalp (CC', g–i). (a) Location map. For each section, we display the V_s structure (b, e and g), the *a posteriori* probability density of interfaces derived from the Bayesian inversion (c, f and h) and their comparison with other geophysical studies (c: from Zhao *et al.* 2015; d: from Solarino *et al.* 2018; f: from Sénéchal & Thouvenot 1991; i: from Kummerow *et al.* 2004). In (c), the black dashed lines indicate the European Moho, the bottom of the Ivrea body and the Adriatic Moho estimated from receiver function analysis along the Cifalps transect. (d) V_p model obtained from local earthquake tomography along Cifalps. (f) Migrated line-drawing of the vertical seismic reflection data (the black dots) and wide-angle seismic reflection data (the black dashed lines) for ECORS-CROP transect (inside the black frame). (i) Migrated receiver function data (blue–red colours) and line-drawing of the controlled-source seismic experiment Transalp. The thick black dashed line indicates the Sub-Tauern ramp.

made a careful selection of measurements according to interstation distance, SNR, similarity of measurements in the causal and acausal sides. 2-D group velocity maps were computed using adaptive parametrization taking into account local path density. In a final step, we inverted local group velocity dispersion curves extracted at each cell for a set of 1-D V_s models. The 1-D inversion follows a two-step data-driven inversion algorithm, with a nonlinear Bayesian inversion followed by a linear least-squares inversion.

Our main methodological improvement is this two-step data-driven inversion algorithm that results in two reliable velocity models without *a priori* information. The first step is a Bayesian inversion that yields a probabilistic model, which results from an exhaustive grid search in a large solution space. It is based on the assumption that at each location, the crust and upper mantle can be described by a four-layer model. It provides the probability distribution of V_s and interface depths. In the second step of the inversion, we extract a final V_s model from the probabilistic model using a linear inversion.

Our final V_s model is so far the highest resolution shear wave velocity model of the European crust derived from ANT ($0.3°$ in the upper crust and $0.9°$ at Moho depth in the Alpine region). Our probabilistic model displays striking similarities with published seismic profiles along three reference cross-sections across the Alpine mountain range, Cifalps, ECORS-CROP and Transalp. It even provides additional information on the crustal structure, for example, in the internal zone of the Alpine orogen where the ECORS-CROP CSS profile failed to probe the deep crust due to the strong reflectivity of the upper crust. A comparison of vertical cross-sections in our two models along the CIFALPS (southwestern Alps) and ECORS-CROP (northwestern Alps) points out unexpected strong differences in the image of the European Moho that deepens continuously towards the northeast along CIFALPS while it displays an ∼8 km Moho jump beneath the inner border of the Belledonne Massif along the ECORS-CROP profile. This illustrates that with a dense network of broad-band stations and using our inversion scheme, ANT can image crustal discontinuities with a similar resolution to that of controlled-source tomography and RF analysis.

Moreover, we probe depths as large as 200 km covering almost the whole lithosphere, thanks to long ray paths (>1500 km) and long-duration noise records for most of the long ray paths. The resulting uppermost mantle structure is in good agreement with earthquake-based tomographic results.

We propose to consider our two models as new reference models of the European crust and uppermost mantle. Our probabilistic model provides probability estimates for layer boundary depths that are potentially of great use in crustal structure studies and geological interpretations, including Moho depth investigations in regions with insufficient station coverage for RF analysis. Our final model, which provides a single *S*-wave velocity at each location is suitable for further geophysical studies including waveform modelling and full-waveform inversion. Both models will be distributed on the authors' website https://sites.google.com/view/seismology-yanglu.

7 ORIGIN OF DATA

Waveform data used in this paper belong to the permanent networks with codes AC, BA, BE (Royal Observatory of Belgium 1985); BN, BS, BW (Department of Earth and Environmental Sciences, Geophysical Observatory, University of Munchen 2001); CA (Institut Cartogràfic i Geològic de Catalunya-Institut d'Estudis Catalans 1996); CH (Swiss Seismological Service (SED) at ETH Zürich

1983); CL (Corinth Rift Laboratory Team And RESIF Datacenter 2013); CQ (Geological Survey Department Cyprus 2013); CR, CZ (Institute of Geophysics, Academy of Sciences of the Czech Republic 1973); DK, DZ, EB, EE, EI (INSN 1993); ES, FN, FR (RESIF 1995); G [Institut De Physique Du Globe De Paris (IPGP) & Ecole Et Observatoire Des Sciences De La Terre De Strasbourg (EOST) 1982]; GB, GE (GEOFON Data Centre 1993); GR, GU (University of Genova 1967); HC (Technological Educational Institute of Crete 2006); HE, HL (National Observatory of Athens, Institute of Geodynamics, Athens 1997); HP (University of Patras, Geology Department, Seismological Laboratory 2000); HT (Aristotle University of Thessaloniki Seismological Network 1981); HU (Kövesligethy Radó Seismological Observatory 1992); IB (Institute Earth Sciences 'Jaume Almera' CSIC (ICTJA Spain) 2007); II (Scripps Institution of Oceanography 1986); IP, IS, IU (Albuquerque Seismological Laboratory (ASL)/USGS 1988); IV (INGV Seismological Data Centre 2006); IX, KO (Bogazici University Kandilli Observatory And Earthquake Research Institute 2001); LC, LX, MD, MN (MedNet Project Partner Institutions, 1990); MT, NI [OGS (Istituto Nazionale di Oceanografia e di Geofisica Sperimentale) and University of Trieste 2002]; NL (KNMI 1993); NO, NS, OE, PL, PM, RD, RO [National Institute for Earth Physics (NIEP Romania) 1994]; SI, SJ, SK [ESI SAS (Earth Science Institute Of The Slovak Academy Of Sciences) 2004]; SL (Slovenian Environment Agency 2001); SS, ST (Geological Survey-Provincia Autonoma di Trento 1981); SX (Leipzig University 2001); TH, TT, TU, UP (SNSN 1904); WM [San Fernando Royal Naval Observatory (ROA), Universidad Complutense De Madrid (UCM), Helmholtz-Zentrum Potsdam Deutsches GeoForschungsZentrum (GFZ), Universidade De Evora (UEVORA, Portugal), & Institute Scientifique of RABAT (ISRABAT, Morocco) 1996]. We also used data of temporary experiments, namely AlpArray (network code Z3_2015; AlpArray Seismic Network 2015), CIFALPS (network code YP_2012; Zhao *et al.* 2016) and PYROPE (network code X7_2010; Chevrot *et al.* 2017).

REFERENCES

Albuquerque Seismological Laboratory (ASL)/USGS, 1988. Global Seismograph Network (GSN - IRIS/USGS). International Federation of Digital Seismograph Networks, Other/Seismic Network, doi:10.7914/SN/IU.

Aristotle University of Thessaloniki Seismological Network, 1981. Permanent Regional Seismological Network operated by the Aristotle University of Thessaloniki. International Federation of Digital Seismograph Networks, Other/Seismic Network, doi:10.7914/SN/HT.

Bodin, T., Sambridge, M., Rawlinson, N. & Arroucau, P., 2012. Trans-dimensional tomography with unknown data noise, *Geophys. J. Int.,* **189**(3), 1536–1556.

Bogazici University Kandilli Observatory And Earthquake Research Institute, 2001. Bogazici University Kandilli Observatory And Earthquake Research Institute. International Federation of Digital Seismograph Networks, Other/Seismic Network, doi:10.7914/SN/KO.

Boschi, L. & Dziewonski, A.M., 1999. High- and low-resolution images of the Earth's mantle: implications of different approaches to tomographic modeling, *J. geophys. Res.,* **104**(B11), 25 567–25 594.

Boschi, L., Fry, B., Ekström, G. & Giardini, D., 2009. The European upper mantle as seen by surface waves, *Surv. Geophys.,* **30**(4–5), 463–501.

Boué, P., Roux, P., Campillo, M. & Briand, X., 2014. Phase velocity tomography of surface waves using ambient noise cross correlation and array processing, *J. geophys. Res.,* **119**(1), 519–529.

Brocher, T.M., 2005. Empirical relations between elastic wavespeeds and density in the Earth's crust, *Bull. seism. Soc. Am.,* **95**(6), 2081–2092.

Campillo, M. & Paul, A., 2003. Long-range correlations in the diffuse seismic coda, *Science,* **299,** 547–549.

Chevrot, S. & Sylvander, M. RESIF, 2017. Seismic network X7: PYROPE PYRenean Observational Portable Experiment (RESIF-SISMOB), RESIF - Réseau Sismologique et géodésique Français, doi:10.15778/resif.x72010.

Closs, H. & Labrouste, Y., 1963, Recherches séismologiques dans les Alpes occidentales au moyen de grandes explosions en 1956, 1958 et 1960, *Mémoire Collectif, Année Géophysique Internationale, C.N.R.S.,* Sér.III, Fasc.2, 236.

Corinth Rift Laboratory Team And RESIF Datacenter, 2013. CL - Corinth Rift Laboratory Seismological Network (CRLNET). RESIF - Réseau Sismologique et géodésique Français, doi:10.15778/resif.cl.

Department of Earth and Environmental Sciences, Geophysical Observatory, University of Munchen, 2001. BayernNetz. International Federation of Digital Seismograph Networks, Other/Seismic Network, doi:10.7914/SN/BW.

Dèzes, P., Schmid, S.M. & Ziegler, P.A., 2004. Evolution of the European Cenozoic Rift System: interaction of the Alpine and Pyrenean orogens with their foreland lithosphere, *Tectonophysics,* **389**, 1–33.

Diehl, T., Husen, S., Kissling, E. & Deichmann, N., 2009. High-resolution 3-D *P*-wave model of the Alpine crust, *Geophys. J. Int.,* **179**(2), 1133–1147.

Dziewonski, A., Bloch, S. & Landisman, M., 1969. A technique for the analysis of transient seismic signals, *Bull. seism. Soc. Am.,* **59**(1), 427–444.

Dziewonski, A.M. & Anderson, D.L., 1981. Preliminary reference Earth model, *Phys. Earth planet. Inter.,* **25**(4), 279–356.

ESI SAS (Earth Science Institute Of The Slovak Academy Of Sciences), 2004. National Network of Seismic Stations of Slovakia. Deutsches GeoForschungsZentrum GFZ, doi:10.14470/fx099882.

Fry, B., Deschamps, F., Kissling, E., Stehly, L. & Giardini, D., 2010. Layered azimuthal anisotropy of Rayleigh wave phase velocities in the European Alpine lithosphere inferred from ambient noise, *Earth planet. Sci. Lett.,* **297**(1–2), 95–102.

GEOFON Data Centre, 1993. GEOFON Seismic Network. Deutsches GeoForschungsZentrum GFZ, doi:10.14470/tr560404.

Geological Survey Department Cyprus, 2013. Cyprus Broadband Seismological Network. International Federation of Digital Seismograph Networks, Other/Seismic Network, doi:10.7914/SN/CQ.

Geological Survey-Provincia Autonoma di Trento, 1981. Trentino Seismic Network. International Federation of Digital Seismograph Networks, Other/Seismic Network, doi:10.7914/SN/ST.

Grad, M. & Tiira, T., 2009. The Moho depth map of the European Plate, *Geophys. J. Int.,* **176**(1), 279–292.

Hansen, P., 2001. The L-curve and its use in the numerical treatment of inverse problems, in *Computational Inverse Problems in Electrocardiography,* Vol. **5,** pp. 119–142, ed. Johnston, P., WIT Press.

Herrmann, R.B., 1973. Some aspects of band-pass filtering of surface waves, *Bull. seism. Soc. Am.,* **63**(2), 663–371.

Herrmann, R.B., 2013. Computer programs in seismology: an evolving tool for instruction and research, *Seismol. Res. Lett.,* **84**(6), 1081–1088.

Hetényi, G. *et al et al,* 2018. The AlpArray Seismic Network: a large-scale European experiment to image the Alpine orogen, *Surv. Geophys.,* doi:10.1007/s10712-018-9472-4.

INGV Seismological Data Centre, 2006. Rete Sismica Nazionale (RSN), Istituto Nazionale di Geofisica e Vulcanologia (INGV), Italy, doi:10.13127/SD/X0FXnH7QfY.

INSN, 1993. Irish National Seismic Network, operated by the Dublin Institute for Advanced Studies and supported by the Geological Survey Ireland. International Federation of Digital Seismograph Networks, Other/Seismic Network, doi:10.7914/SN/EI.

Institut Cartogràfic i Geològic de Catalunya-Institut d'Estudis Catalans, 1996. Catalan Seismic Network. International Federation of Digital Seismograph Networks, Other/Seismic Network, doi:10.7914/SN/CA.

Institut De Physique Du Globe De Paris (IPGP), & Ecole Et Observatoire Des Sciences De La Terre De Strasbourg (EOST), 1982. GEOSCOPE - French Global Network of broadband seismic stations - Institut de Physique du Globe de Paris, doi:10.18715/geoscope.g.

Institute Earth Sciences "Jaume Almera" CSIC (ICTJA Spain), 2007. IberArray. International Federation of Digital Seismograph Networks, Other/Seismic Network, doi:10.7914/SN/IB.

Institute of Geophysics, Academy of Sciences of the Czech Republic, 1973. Czech Regional Seismic Network. International Federation of Digital Seismograph Networks, Other/Seismic Network, doi:10.7914/SN/CZ.

KNMI, 1993. Netherlands Seismic and Acoustic Network. Royal Netherlands Meteorological Institute (KNMI). Other/Seismic Network, doi:10.21944/e970fd34-23b9-3411-b366-e4f72877d2c5.

Köveslégethy Radó Seismological Observatory, 1992. Hungarian National Seismological Network. Deutsches GeoForschungsZentrum GFZ. Other/Seismic Network, doi:10.14470/UH028726.

Kummerow, J., Kind, R., Oncken, O., Giese, P., Ryberg, T., Wylegalla, K. & Scherbaum, F., 2004. A natural and controlled source seismic profile through the Eastern Alps: TRANSALP, *Earth planet. Sci. Lett.,* **225**(1–2), 115–129.

Larose, E. *et al.*, 2006. Correlation of random wavefields: an interdisciplinary review, *Geophysics,* **71**(4), SI11–SI21.

Laske, G., Masters, G., Ma, Z. & Pasyanos, M., 2013. Update on CRUST1.0 - a 1-degree global model of Earth's crust, in *Geophysical Research Abstracts EGU General Assembly,* Vienna, Austria, Vol. **15,** pp. 2013–2658.

Legendre, C.P., Meier, T., Lebedev, S., Friederich, W. & Viereck-Götte, L., 2012. A shear wave velocity model of the European upper mantle from automated inversion of seismic shear and surface waveforms, *Geophys. J. Int.,* **191**(1), 282–304.

Leipzig University, 2001. SXNET Saxon Seismic Network. International Federation of Digital Seismograph Networks, Other/Seismic Network, doi:10.7914/SN/SX.

Levshin, A.L., Yanovskaya, T.B., Lander, A.V., Bukchin, B.G., Barmin, M.P., Ratnikova, L.I. & Its, E.N., 1989. in *Seismic Surface Waves in a Laterally Inhomogeneous Earth, Modern Approaches in Geophysics,* Vol. **9,** Springer Netherlands.

Li, H., Bernardi, F. & Michelini, A., 2010. Surface wave dispersion measurements from ambient seismic noise analysis in Italy, *Geophysics. J. Int.,* **180**(3), 1242–1252.

Ludwig, W., Nafe, J. & Drake, C., 1970. Seismic refraction, in *the Sea,* Vol. **4**(Part 1), pp. 53–84, Maxwell, A.E., Wiley-Interscience.

Lüschen, E., Lammerer, B., Gebrande, H., Millahn, K. & Nicolich, R., 2004. Orogenic structure of the Eastern Alps, Europe, from TRANSALP deep seismic reflection profiling, *Tectonophysics,* **388**(1–4), 85–102.

Macquet, M., Paul, A., Pedersen, H.A., Villaseñor, A., Chevrot, S., Sylvander, M. & Wolyniec, D., 2014. Ambient noise tomography of the Pyrenees and the surrounding regions: inversion for a 3-D V_s model in the presence of a very heterogeneous crust, *Geophys. J. Int.,* **199**(1), 402–415.

MedNet Project Partner Institutions, 1990. Mediterranean Very Broadband Seismographic Network (MedNet). Istituto Nazionale di Geofisica e Vulcanologia (INGV), Italy, doi:10.13127/sd/fbbbtdtd6q.

Molinari, I. & Morelli, A., 2011. EPcrust: a reference crustal model for the European Plate, *Geophys. J. Int.,* **185**(1), 352–364.

Molinari, I., Verbeke, J., Boschi, L., Kissling, E. & Morelli, A., 2015. Italian and Alpine three-dimensional crustal structure imaged by ambient-noise surface-wave dispersion, *Geochem. Geophys. Geosyst.,* **16**(12), 4405–4421.

National Institute for Earth Physics (NIEP Romania), 1994. Romanian Seismic Network. International Federation of Digital Seismograph Networks, Other/Seismic Network, doi:10.7914/SN/RO.

National Observatory of Athens, Institute of Geodynamics Athens, 1997. National Observatory of Athens Seismic Network. International Federation of Digital Seismograph Networks, Other/Seismic Network, doi:10.7914/SN/HL.

Nicolas, A., Hirn, A., Nicolich, R. & Polino, R., 1990. Lithospheric wedging in the western Alps inferred from the ECORS-CROP traverse, *Geology,* **18**(7), 587–590.

OGS (Istituto Nazionale di Oceanografia e di Geofisica Sperimentale) and University of Trieste, 2002. North-East Italy Broadband Network. International Federation of Digital Seismograph Networks, Other/Seismic Network, doi:10.7914/SN/NI.

Paige, C.C. & Saunders, M.A., 1982. LSQR: an algorithm for sparse linear equations and sparse least squares, *Trans. Math. Softw.,* **8**(1), 43–71.

Paul, A., Cattaneo, M., Thouvenot, F., Spallarossa, D., Béthoux, N. & Fréchet, J., 2001. A three-dimensional crustal velocity model of the southwestern Alps from local earthquake tomography, *J. geophys. Res.,* **106**(B9), 19 367–19 389.

Pedersen, H.A. & Krüger, F., 2007. Influence of the seismic noise characteristics on noise correlations in the Baltic shield, *Geophys. J. Int.,* **168**(1), 197–210.

Pfiffner, O.A., Lehner, P., Heitzmann, P., Mueller, S. & Steck, A., 1997. *Deep Structure of the Swiss Alps: Results of NRP 20,* Birkhäuser.

Pharaoh, T.C., 1999. Paleozoic terranes and their lithospheric boundaries within the Trans-European Suture Zone (TESZ): a review, *Tectonophysics,* **314,** 17–41.

Piana Agostinetti, N. & Amato, A., 2009. Moho depth and V_p/V_s ratio in peninsular Italy from teleseismic receiver functions, *J. geophys. Res.,* **114**(B6), B06303, doi:10.1029/2008JB005899.

Platt, J.P., 2007. From orogenic hinterlands to Mediterranean-style back-arc basins: a comparative analysis, *J. Geol. Soc.,* **164,** 297–311.

RESIF, 1995. RESIF-RLBP French Broad-band network, RESIF-RAP strong motion network and other seismic stations in metropolitan France. RESIF - Réseau Sismologique et géodésique Français, doi:10.15778/resif.fr.

Royal Observatory of Belgium, 1985. Belgian Seismic Network. International Federation of Digital Seismograph Networks, Other/Seismic Network, doi:10.7914/SN/BE.

Roux, P., Sabra, K.G., Gerstoft, P., Kuperman, W.A. & Fehler, M.C., 2005. *P*-waves from cross-correlation of seismic noise, *Geophys. Res. Lett.,* **32**(19), L19303, doi:10.1029/2005GL023803.

San Fernando Royal Naval Observatory (ROA), Universidad Complutense De Madrid (UCM), Helmholtz-Zentrum Potsdam Deutsches GeoForschungsZentrum (GFZ), Universidade De Evora (UEVORA, Portugal), & Institut Scientifique of RABAT (ISRABAT, Morocco), 1996. The Western Mediterranean BB seismic Network, Deutsches GeoForschungsZentrum GFZ, doi:10.14470/jz581150.

Sánchez-Sesma, F.J., Pérez-Ruiz, J.A., Campillo, M. & Luzón, F., 2006. Elastodynamic 2-D Green function retrieval from cross-correlation: canonical inclusion problem, *Geophys. Res. Lett.,* **33**(13), L13305, doi:10.1029/2006GL026454.

Schaefer, J.F., Boschi, L. & Kissling, E., 2011. Adaptively parametrized surface wave tomography: methodology and a new model of the European upper mantle, *Geophys. J. Int.,* **186**(3), 1431–1453.

Schivardi, R. & Morelli, A., 2011. EPmantle: a 3-D transversely isotropic model of the upper mantle under the European Plate, *Geophys. J. Int.,* **185**(1), 469–483.

Scripps Institution of Oceanography, 1986. IRIS/IDA Seismic Network. International Federation of Digital Seismograph Networks, Other/Seismic Network, doi:10.7914/SN/II.

Sénéchal, G. & Thouvenot, F., 1991. Geometrical migration of line-drawings: a simplified method applied to ECORS data, in *Continental Lithosphere: Deep Seismic Reflections,* pp. 401–407, eds Meissner, R., Brown, L., Dürbaum, H.-J., Franke, W., Fuchs, K. & Seifert, F., American Geophysical Union.

Shen, W., Ritzwoller, M.H., Schulte-Pelkum, V. & Lin, F.C., 2013. Joint inversion of surface wave dispersion and receiver functions: a Bayesian Monte-Carlo approach, *Geophys. J. Int.,* **192**(2), 807–836.

Slovenian Environment Agency, 2001. Seismic Network of the Republic of Slovenia. International Federation of Digital Seismograph Networks, Other/Seismic Network, doi:10.7914/SN/SL.

SNSN, 1904. Swedish National Seismic Network, Uppsala University, Uppsala, Sweden, doi:10.18159/snsn.

Solarino, S. *et al.*, 2018. Mantle wedge exhumation beneath the Dora-Maira (U)HP dome unravelled by local earthquake tomography (Western Alps), *Lithos,* **296–299,** 623–636.

Spada, M., Bianchi, I., Kissling, E., Agostinetti, N.P. & Wiemer, S., 2013. Combining controlled-source seismology and receiver function information to derive 3-D Moho topography for Italy, *Geophys. J. Int.,* **194**(2), 1050–1068.

Spakman, W. & Bijwaard, H., 2001. Optimization of cell parameterizations for tomographic inverse problems, *Pure appl. Geophys.,* **158**(8), 1401–1423.

Stehly, L., Campillo, M. & Shapiro, N.M., 2006. A study of the seismic noise from its long-range correlation properties, *J. geophys. Res.,* **111**(B10), B10306, doi:10.1029/2005JB004237.

Stehly, L., Fry, B., Campillo, M., Shapiro, N.M., Guilbert, J., Boschi, L. & Giardini, D., 2009. Tomography of the Alpine region from observations of seismic ambient noise, *Geophys. J. Int.,* **178**(1), 338–350.

Swiss Seismological Service (SED) at ETH Zürich, 1983. National Seismic Networks of Switzerland; ETH Zürich. Other/Seismic Network, doi:10.12686/sed/networks/ch.

Technological Educational Institute of Crete, 2006. Seismological network of Crete. International Federation of Digital Seismograph Networks, Other/Seismic Network, doi:10.7914/SN/HC.

Tesauro, M., Kaban, M. & Cloetingh, S., 2008. EuCRUST-07: a new reference model for the European crust, *Geophys. Res. Lett.,* **35,** L05313, doi:10.1029/2007GL032244.

Thouvenot, F., Paul, A., Sénéchal, G., Hirn, A. & Nicolich, R., 1990. ECORS-CROP wide-angle reflection seismics: constraints on deep interfaces beneath the Alps, *Mem. Soc. geol. Fr.,* **156,** 97–106.

University of Genova, 1967. Regional Seismic Network of North Western Italy. International Federation of Digital Seismograph Networks, Other/Seismic Network, doi:10.7914/SN/GU.

University of Patras, Geology Department Seismological Laboratory, 2000. PSLNET, permanent seismic network operated by the University of Patras, Greece. International Federation of Digital Seismograph Networks, Other/Seismic Network, doi:10.7914/SN/HP.

Verbeke, J., Boschi, L., Stehly, L., Kissling, E. & Michelini, A., 2012. High-resolution Rayleigh-wave velocity maps of central Europe from a dense ambient-noise data set, *Geophys. J. Int.,* **188**(3), 1173–1187.

Waldhauser, F., Kissling, E., Ansorge, J. & Mueller, S., 1998. Three-dimensional interface modelling with two-dimensional seismic data: the Alpine crust–mantle boundary, *Geophys. J. Int.,* **135**(1), 264–278.

Wapenaar, K., 2004. Retrieving the elastodynamic Green's function of an arbitrary inhomogeneous medium by cross correlation, *Phys. Rev. Lett.,* **93**(25), 1–4.

Weaver, R.L. & Lobkis, O.I., 2001. Ultrasonics without a source: thermal fluctuation correlations at MHz frequencies, *Phys. Rev. Lett.,* **87**(13), 134301, doi:10.1103/PhysRevLett.87.134301.

Weaver, R.L. & Lobkis, O.I., 2002. On the emergence of the Green's function in the correlations of a diffuse field: pulse-echo using thermal phonons, *Ultrasonics,* **40**(1-8), 435–439.

Yang, Y. & Ritzwoller, M.H., 2008. Characteristics of ambient seismic noise as a source for surface wave tomography, *Geochem. Geophys. Geosyst.,* **9**(2), Q02008, doi:10.1029/2007GC001814.

Yang, Y., Ritzwoller, M.H., Levshin, A.L. & Shapiro, N.M., 2007. Ambient noise Rayleigh wave tomography across Europe, *Geophys. J. Int.,* **168**(1), 259–274.

Zhao, L. *et al.,* 2015. First seismic evidence for continental subduction beneath the Western Alps, *Geology,* **43**(9), 815–819.

Zhao, L., Paul, A. & Solarino, S. RESIF, 2016. Seismic network YP: CIFALPS temporary experiment (China–Italy–France Alps seismic transect), RESIF - Réseau Sismologique et géodésique Français, doi:10.15778/RESIF.YP2012.

Zhu, H., Bozdag, E. & Tromp, J., 2015. Seismic structure of the European upper mantle based on adjoint tomography, *Geophys. J. Int.,* **201**(1), 18–52.

Shapiro, N.M., Campillo, M., Stehly, L. & Ritzwoller, M.H., 2005. High-resolution surface wave tomography from ambient seismic noise, *Science,* **307,** 1615–1618.

SUPPORTING INFORMATION

Supplementary data are available at *GJI* online.

Figure S1. Histogram of the number of months used to compute the stacked correlations.

Figure S2. Stacked cross-correlation functions for station pairs including station CH.DAVOX in the period bands 20–40 s (top) and 80–150 s (bottom).

Figure S3. Resolution assessment of group velocity maps using multiscale checkerboard tests. (1a–c) input models with velocity anomalies of sizes 0.6°, 1.8° and 5.4°; (2a–c) outputs for period 8 s; (3a–c) outputs for period 40 s; (4a–c) outputs for period 125 s. The black dashed lines in panels (2a), (3b) and (4c) enclose areas with resolution better than 0.6°, 1.8° and 5.4° at 8, 40 and 125 s, respectively.

Figure S4. Uncertainty assessments of inversion for group velocity maps using Jackknifing tests at periods 8, 40 and 125 s. Arbitrarily selected 80 per cent of the original data are used to invert for group velocity maps. This procedure is iterated 30 times. Standard deviations of the ensemble of results are plotted to document the inversion uncertainty. The analysis of results should be limited to the area well sampled by data, which means simultaneously good data coverage and good data azimuthal distribution.

Figure S5. Group velocity maps at periods 5, 15, 25 and 75 s. We plot only cells crossed by more than 10 paths.

Figure S6. Rms errors of inversion results for period bands 5–15 s (a), 15–55 s (b) and 55–150 s (c). We plot only cells with more than 10 crossing paths at 8 s.

Figure S7. Depth slices in the final V_s model at 5, 20, 40 and 75 km. We plot only cells crossed by more than 10 paths at 8 s period. Moreover, we discard cells with rms error greater than 0.06 km s^{-1} (see Fig. S5).

Figure S8. 3-D views of the Bayesian Moho depth map in the greater Alpine region (map view in Fig. 8d).

Please note: Oxford University Press is not responsible for the content or functionality of any supporting materials supplied by the authors. Any queries (other than missing material) should be directed to the corresponding author for the paper.